

1 **Characterizing the evolution of mass flow properties and dynamics through analysis of**
2 **seismic signals: Insights from the 18 March 2007 Mt. Ruapehu lake-breakout lahar**

3

4 Braden Walsh¹, Charline Lormand², Jon Procter³, Glyn Williams-Jones¹

5 ¹Department of Earth Sciences, Simon Fraser University, Burnaby, British Columbia, Canada

6 ²Department of Earth Sciences, University of Durham, Durham, DH1 3LE, UK

7 ³Volcanic Risk Solutions, Institute of Agriculture and Environment, Massey University,

8 Palmerston North, New Zealand

9

10 Corresponding Author: Braden Walsh (braden_walsh@sfu.ca)

11

12 **Abstract**

13 Monitoring for mass flows, on volcanoes can be challenging due to the ever-changing landscape

14 along the flow path, which can drastically transform the properties and dynamics of the flow.

15 These changes to the flows require the need for detection strategies and risk assessment that

16 are tailored not only between different volcanoes, but at different distances along flow paths as

17 well. Being able to understand how a flow event may transform in time and space along the

18 channel is of utmost importance for hazard management. While visual observations and simple

19 measuring devices in the past have shown how volcanic mass flows transform along the flow

Deleted: lahars

Deleted: lahars

22 path, these same features for the most part have not been described using seismological
23 methods. On 18 March 2007, Mt. Ruapehu produced the biggest lahar in New Zealand in over
24 100 years. At 23:18 UTC the tephra dam holding the Crater Lake water back collapsed causing
25 $1.3 \times 10^6 \text{ m}^3$ of water to flow out and rush down the Whangaehu channel. We describe here the
26 seismic signature of a lake-breakout lahar over the course of 83 km along the Whangaehu river
27 system using three 3-component broadband seismometers installed <10 m from the channel at
28 7.4, 28, and 83 km from the crater lake source. Examination of 3-component seismic
29 amplitudes, frequency content, and directionality, combined with video imagery and sediment
30 concentration data were used. The seismic data shows the evolution of the lahar as it
31 transformed from a highly turbulent out-burst flood (high peak frequency throughout), to a
32 fully bulked up multi-phase hyperconcentrated flow (varying frequency patterns depending on
33 the lahar phase) to a slurry flow (bedload dominant). Estimated directionality ratios show the
34 elongation of the lahar with distance down channel, where each recording station depicts a
35 similar pattern, but for differing lengths of time. Furthermore, using directionality ratios shows
36 extraordinary promise for lahar monitoring and detection systems where streamflow is present
37 in the channel.

Deleted: 5

Deleted: shows

38 1. Introduction

39 Volcanic mass flows (e.g. debris flows, pyroclastic density currents, debris avalanches,
40 hyperconcentrated flows) are one of the greatest threats to communities, industry, recreation,
41 etc. on and around volcanoes. Volcanic mass flows are particularly dangerous as they are fast
42 moving turbulent flows that can occur without any warning or an eruption transpiring (Capra et

Deleted: These

Deleted: v

47 al., 2010). These flows can move a sizable amount of liquid and debris great distances that can
48 critically impact locations hundreds of kilometers from the volcano or source. Lake-breakout or
49 outburst flood events can be particularly destructive because they tend to be larger and can
50 cause long lasting changes to the landscape and surrounding ecosystems (O'Connor et al., 2013;
51 Procter et al., 2021). Furthermore, unlike eruption or rain triggered mass flows, outburst floods
52 have very little to no warning. Eruption triggered flows can be prepared for by the onset of the
53 eruption and/or the monitoring of the volcano through various methods (e.g. seismology,
54 infrasound, gravity, gas and water chemistry). Likewise, for rain-induced flows using techniques
55 such as measuring the amount or intensity of rain (e.g. Capra et al., 2010; 2018) or by
56 monitoring the amount of available material (e.g. Iguchi, 2019) can help forecast when an event
57 may occur.

Deleted: sources

58 In New Zealand, there have been numerous cases of large damaging mass flows in modern
59 times. For example, in October 2012, a lake-breakout lahar originating from Te Maari,
60 destroyed hiking trails and forestry, eventually flowing over 4.5 km to damage and block off
61 Highway 46 (Procter et al., 2014; Walsh et al., 2016). Moreover, on 24 December 1953, the
62 deadliest volcanic mass flow in New Zealand history occurred killing 151 people when a lahar
63 struck a train crossing at the Tangiwai Rail Bridge, 39.8 km from the Crater Lake on top of Mt.
64 Ruapehu (O'Shea, 1954). The ability to predict and investigate the changing dynamics and
65 properties of large volcanic mass flows as they progress down channel is the first step in
66 beginning to understand flow mechanisms better, and ultimately address the hazards involved
67 to mitigate the risk.

Deleted: i

Deleted: lahar

71 In order to better characterize and understand these flow events, many [in-situ](#) applications and
72 instruments have been used in the past (e.g. trip wires, stage gauge, load cells, pore pressure).
73 While many of these tools can yield quick assessments and provide ample warning (e.g. current
74 meters, trip wires), they can sometimes be at risk of false detections, equipment damage or
75 loss, and/or lack the capability to evaluate multiple pulses or flow events ([Arattano et al., 1999](#)).
76 Geophysical instruments (e.g. seismometers, geophones, infrasound) on the other hand can be
77 installed at a safe distance away from the channel and have shown signs of not only being
78 capable warning systems (e.g. Coviello et al., 2019), but have the ability to accurately estimate
79 flow properties (e.g. Arattano and Marchi, 2005; Doyle et al., 2010; Schimmel et al., 2021), as
80 well as flow dynamics (e.g. Gimbert et al., 2014; Coviello et al., 2018; Walsh et al., 2020).
81 However, in order to fully utilize these instruments, improved interpretation, comprehension,
82 assessment, and universality is needed. One technique to increase the ability to predict, warn,
83 and estimate the properties and dynamics of flow events is to use all three components of the
84 seismic recording. Recently, several studies have shown that using all three components is
85 effective in characterizing flow events (e.g. snow-slurry lahars, Cole et al., 2009; snow
86 avalanches, Kogelnig et al., 2011; streamflow, Roth et al., 2016; landslides, Surinach et al., 2005;
87 lahars, Walsh et al., 2020; rockfalls, Kuehnert et al., 2021; hyperconcentrated flows, Walsh et
88 al., 2016). Using the horizontal components along with the vertical component can yield
89 additional information about the flow that is not utilized if only the vertical component is used.
90 Notably, directionality ([cross-channel over channel-parallel](#)) analysis (e.g. Doyle et al., 2010;
91 Walsh et al., 2020) can provide information about [the](#) wetted perimeter, sediment
92 concentration, and number of particle collisions. Furthermore, differing energies and frequency

93 outputs from channel parallel and channel perpendicular signals can point to specific changes
94 within the flow (Burtin et al., 2010; Roth et al., 2016) that can provide insights into the internal
95 dynamics.

96 1.1 Anatomy of lahars

97 When a lahar is created from a lake-breakout or outburst flood event, the transition from flood
98 or streamflow torrent depends on the erosivity of the channel and the supply of sediment being

99 entrained within the flow (e.g. Scott, 1988; Doyle et al., 2011). An event may start as a highly
100 turbulent low sediment flow, then transform into a hyperconcentrated flow, and may even

101 eventually 'bulk up' to exhibit characteristics of a debris flow with the possibility of plug-like
102 (limited internal motion and collisions) or laminar behavior (Scott, 1988, Pierson et al., 1990). At

103 Mt. Ruapehu, the propagational differences of lahars down channel have been observed and
104 characterized in the past (e.g. Cronin et al., 1996; Cronin et al., 1999; Cronin et al., 2000;

105 Manville et al., 2000; Procter et al., 2010a; Lube et al., 2012). From these studies, models of
106 how lahars bulk up and transition throughout the run-out distance have been postulated. For

107 the lahars in the Whangaehu channel, Cronin et al. (1999) created three 4-phase conceptual
108 models based on source distances of 23.5 km, 42 km, and >55 km. The first two models are for

109 lahar regimes, whereas the third model described a lahar almost at its peak run-out distance. In
110 each model, the first phase consists of a super charged streamflow pulse that flows ahead of

111 the head of the flow and is considered the front of the lahar. This phenomenon has also been
112 noted for debris flows interacting with streamflow (Arattano and Moia, 1999). Furthermore,

113 discharge is maximum at the transition between phase 1 and phase 2 (Cronin et al., 1999), and

Deleted: rapped

Deleted: laminar or

116 is described as the head of the flow. Phase 2 is described as a mixing zone between streamflow
117 and increasing sediment content, where the peak sediment concentration usually occurs at the
118 end of phase 2 or at the beginning of phase 3 (e.g. Pierson and Scott, 1985). Cronin et al. (1999)
119 defined phase 3 as the lahar body, which has the least amount of the original streamflow
120 contained within. Phase 3 is also characterized by coarse sediment suspensions and is the most
121 likely location for debris flow rheology. Finally, phase 4 is the tail of the lahar where debulking
122 and dilution occurs transforming the lahar back into a hyperconcentrated, mixed, or
123 streamflow.

Deleted: .

124 **1.2 18 March 2007 lake-breakout event**

125 Mt. Ruapehu (2797 asl) is the largest stratovolcano in the central North Island of New Zealand
126 (Figure 1) which sits at the southwestern end of the Taupō Volcanic Zone (TVZ). The volcano has
127 a volume of 110 km³ which is composed of several overlapping cone building formations and
128 surrounding ring plain volcanoclastics (Carrivick et al., 2009; Pardo et al., 2012). On top of the
129 volcano, above the currently active vent sits a 1x10⁷ m³ acidic crater lake (Procter et al., 2010a).
130 The Whangaehu channel is the preferred outlet for Crater Lake water and lahars in recent
131 history (Procter et al., 2012; Procter et al., 2021). The Whangaehu channel is on the eastern
132 flank of Mt. Ruapehu where it runs down across the volcanic ring plane and eventually heads
133 southwest for ~200 km reaching the Tasman Sea (Figure 1).

Deleted: where it

134 Prior to the events that took place in the morning local time on 18 March 2007, a heavy
135 rainstorm occurred accumulating about 256 mm of water over the 10 hours prior to the dam
136 breach that led to the outburst flood (Massey et al., 2010). The intense rain caused the Crater

139 Lake to rise an extra 6.4 m and overtop the natural lava formation ledge, which started to cause
140 seepage and extra water to enter the Whangaehu gorge (Carrivick et al., 2009). At ~~~23~~;18 UTC,
141 the tephra dam collapsed causing 1.3×10^6 m³ of water to flow out of the lake and into the
142 Whangaehu channel (Procter et al., 2010a). The dam was eroded and undercut in multiple
143 stages resulting in a series of retrogressing landslides along with the main debris flow/lahar,

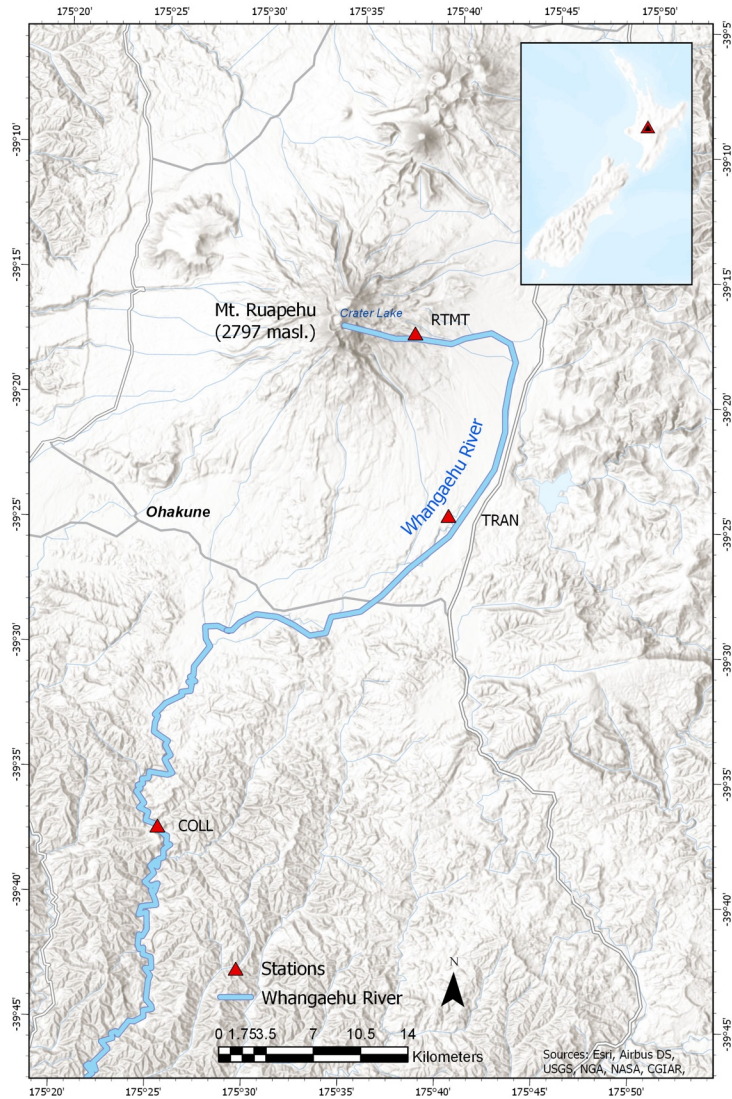
Deleted: above

Deleted: entering

Deleted: 11

Deleted: NZT (UTC +12)

Deleted: channel



149

150 Figure 1 Map of Mt. Ruapehu and the surrounding area located on the central North Island of New Zealand. Blue
 151 outline represents the Whangaehu channel and the path the 18 March 2007 lahar traveled down. Red triangles
 152 denotes the three monitoring stations along the Whangaehu channel at 7.4, 28, and 83 km.

153 Since the lahar was caused by lake-breakout dynamics and thus **contained** an abundance of
154 water, the event was classified as a hyperconcentrated streamflow (Procter et al., 2010b). At
155 ~8.0 km from source, **the lahar** velocity **was** recorded at ~ 9.5 m/s and had an estimated 6 m of
156 downcutting, showing the **capability of** the lahar to deposit and erode massive amounts of
157 material (Procter et al., 2010a,b). Furthermore, the 18 March 2007 lahar was one of the most
158 thoroughly monitored lahars ever (Manville and Cronin 2007). In total there were 21
159 monitoring locations (**only three of which had 3-component seismometers**) setup to measure
160 various lahar properties, (e.g. flow monitor, camera, stage height, flow sampling, pore-
161 pressure, seismic, etc.) along the channel (Keys and Green, 2008; Lube et al., 2012), with the
162 lahar taking over 16 hours to eventually travel out to the New Zealand coast, ~200 km from the
163 original crater lake source.

Deleted: rather than a sediment-filled debris flow

Deleted: measurements

Deleted: the flow

Deleted: ability

Deleted: for

164 Here, we delve into the properties of **the 18 March 2007** lake-breakout hyperconcentrated
165 streamflow that bulked up to a volume of $\sim 4.4 \times 10^6 \text{ m}^3$ (Procter et al., 2010a) over the course of
166 83 km **along the Whangaehu channel**, originating from Mt. Ruapehu, New Zealand. The
167 combination of seismic analysis (frequency and directionality) with supplementary
168 measurements (e.g. video, sediment concentration) show how a lahar transforms over time and
169 distance and how using these seismic techniques can help monitor the ever changing dynamics
170 and properties of a flow event. Furthermore, we examine previous models of the evolution of a
171 lahar and compare the model with the seismic data available.

Deleted: a

Deleted: that occurred on 18 March 2007

172 2. Data

180 The seismic data for the 18 March 2007 lahar was recorded on three seismometers installed at
181 various distances (7.4, 28, 83 km) along the Whangaehu channel (Figure 1). The data from the
182 three 3-component broadband Guralp 6T sensors (COLL, RTMT, TRAN) were recorded using a
183 sampling rate of 100 Hz and GPS time stamps. For each site, the seismometers axes were
184 installed to true North and the recorded data were rotated to align North as flow parallel (P)
185 and East as the cross-channel direction (T). The seismic data were rotated to align with the
186 channel in order to determine the differences in energy output between the flow parallel and
187 cross-channel directions (e.g. directionality). The monitoring station Round the Mountain Track
188 (RTMT), was installed 4 m from the channel and 7.4 km downstream from the source of the
189 lahar. The lahar arrived at RTMT at 23:36 UTC and had an average velocity of 9.3 m/s (Figure
190 2a). The Trans Rail Gauge (TRAN) station was installed 28 km from source and 10 m from the
191 channel, which also included a video camera that captured an image every 30 seconds. The
192 lahar arrived at TRAN at 24:35 UTC and had an average velocity of 5.6 m/s (Figure 2d). The
193 Colliers Bridge (COLL) station was installed 10 m from the channel and 83 km from source. The
194 lahar arrived at COLL at 04:13 UTC and had an average velocity of 4.8 m/s (Figure 2f). Arrival
195 times are based off of images and eye witnesses at each of the monitoring stations. The flow
196 velocity at RTMT and COLL were estimated from imagery and at TRAN from a flow meter.
197 Sediment concentration at COLL was measured manually through dip buckets.

198 3. Results

199 To examine the multi-component dynamics of the 18 March 2007 lake-breakout event along
200 the Whangaehu channel at three monitoring locations, the data were corrected for instrument

Deleted: recorded data at

Deleted: sampling and had

Deleted: Furthermore, the seismometers were installed normal to horizontal to lessen the degree of vertical energy transfer to the horizontal components.

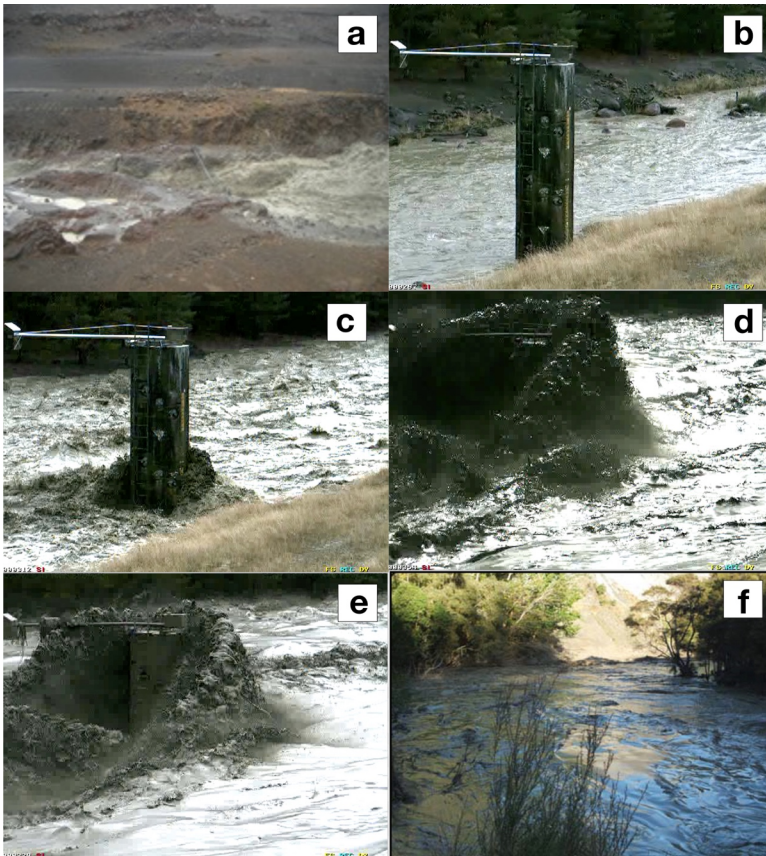
Deleted: with

207 response and split into 10 s time windows. At each recording location, peak spectral frequency
208 (PSF), root mean squared (RMS) amplitude, and directionality ratios (DR) are estimated for each
209 of the 10 s time windows ([Table S1](#)). At each monitoring station the first hour of the lahar
210 including five minutes prior to the arrival are shown in all the results except when indicated.

211

212

Deleted: amplitude



214

215 *Figure 2 Images from the 18 March 2007 lake break-out lahar from RTMT (a), TRAN (b, c, d, e), and COLL (f). Note*
 216 *the transformation of the lahar at TRAN from streamflow (b), increased discharge pre-lahar phase 1 pulse/**flow*
 217 *front (bow wave) (c), head of the lahar (**peak seismic amplitude**) (d), and low PSF beginning of lahar body (**see*
 218 *figure 4 after 15 minute mark) (e).*

219 **3.1 Frequency analysis**

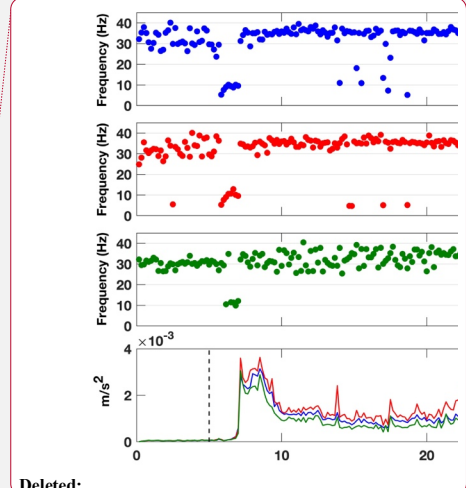
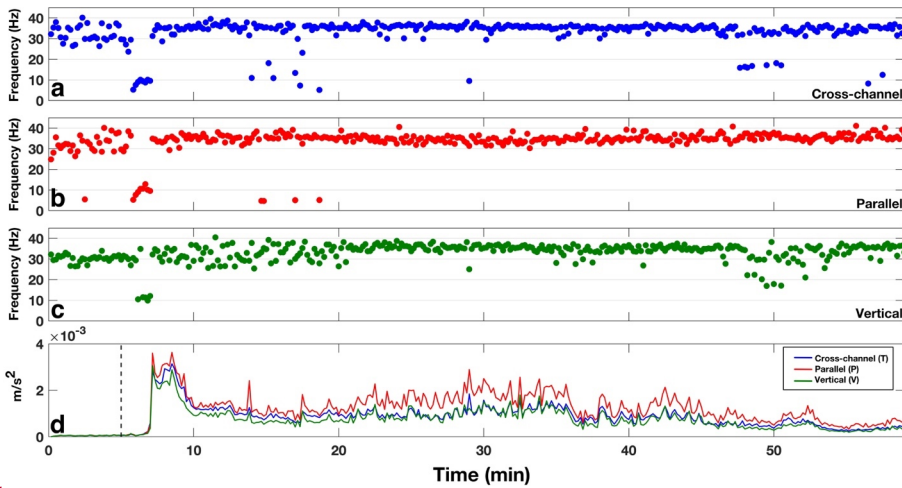
220 In order to examine the PSFs for all three components at each site along the channel, we use

221 the frequency recorded at the maximum amplitude of the frequency spectra for each 10 s

222 running time window (*i.e. non-overlapping windowed FFT*). The PSF for RTMT (7.4 km from

223 source) shows similar patterns between all three components (Figure 3). The five minutes prior
 224 to the arrival of the front of the lahar are characterized by scattered PSFs between 20-40 Hz for
 225 the cross-channel (Figure 3a) and parallel (Figure 3b) directions, while in the vertical direction
 226 (Figure 3c) the PSF is ~30 Hz. When the front (streamflow pulse/bow wave) of the lahar arrives
 227 at the station, the PSF in all three components decreases to ~5-10 Hz for about 1 min before
 228 increasing again to higher frequencies. After the head (peak seismic amplitude) of the lahar
 229 passes the station, the PSF in the cross-channel and parallel directions remain between 30-40
 230 Hz for the rest of the recording window. In the vertical component, the PSF is scattered
 231 between 20-40 Hz for ~15 min after the arrival of the head of the lahar and then becomes
 232 narrower, similar to both the cross-channel and parallel components with PSFs between 30-40
 233 Hz.

- Deleted: five
- Deleted: head
- Deleted: (peak seismic amplitude)
- Deleted: , blue dots
- Deleted: 2
- Deleted: , red dots
- Deleted: , green dots
- Deleted: front
- Deleted: and when the head arrives



234
 235 Figure 3 Peak spectral frequencies for RTMT (7.4 km from source) for a) cross-channel (blue), b) flow parallel (red),
 236 and c) vertical (green) directions. Bottom row d) depicts the RMS amplitude of the lahar color coded to the same

- Deleted:
- Deleted: dots
- Deleted: dots
- Deleted: n dots

250 colors as the PSF. The dashed vertical line marks the timing of the lahar front passing the monitoring station. All
251 PSFs and RMS amplitudes were calculated using 10 s time windows.

252 Further down the channel at station TRAN (28 km from source), the PSFs for all three
253 components show a similar overall pattern (Figure 4). The pre-lahar PSF distribution in all three
254 components is between 20-32 Hz. Like RTMT higher up the channel, the PSFs for the front of
255 the lahar at TRAN drops down to around 10 Hz and when the lahar head arrives (~10 min,
256 Figure 4) the PSF increases to ~30 Hz for parallel (Figure 4b) and cross-channel (Figure 4a)
257 directions and between 20-30 Hz in the vertical component (Figure 4c). This decrease to lower
258 frequencies before the head of the lahar at TRAN lasts for about 5 min. After the head of the
259 lahar passes the recording station the PSF content decreases for ~15 min to 10-20 Hz for the
260 parallel and cross-channel components and between 10-25 Hz for the vertical components. The
261 PSF after the 30 minute mark in Figure 4 displays a bimodal pattern with frequencies between
262 10-35 Hz, with PSF time windows concentrating most at ~30 Hz.

263 At the COLL recording station (83 km from source), the PSF distribution shows differing patterns
264 for all three components (Figure 5). The PSF in the cross-channel direction (Figure 5a) depicts a
265 bimodal pattern throughout with a strong lower concentration of time windows at ~18 Hz and a
266 higher PSF at ~25 Hz. For the parallel component (Figure 5b), the pre-lahar signal has a wide PSF
267 range between 12-30 Hz. When the lahar arrives, the PSF becomes concentrated at ~22 Hz for
268 ~8 min before transforming into a bimodal pattern similar to that of the cross-channel PSF, with
269 frequencies between 20-30 Hz. In the vertical component (Figure 5c), the pre-lahar PSF is
270 scattered between 22-30 Hz, then as the front of the lahar passes the station, the PSF stabilizes
271 around 28 Hz for about 12 min. When the lahar head arrives, the PSF again transitions to more
272 of a scattered pattern during the highest energy stage of the lahar (Figure 5, 25-40 min).

Deleted: first

Deleted: , red dots

Deleted: , b

Deleted: lue dots

Deleted: (Figure 4, green dots)

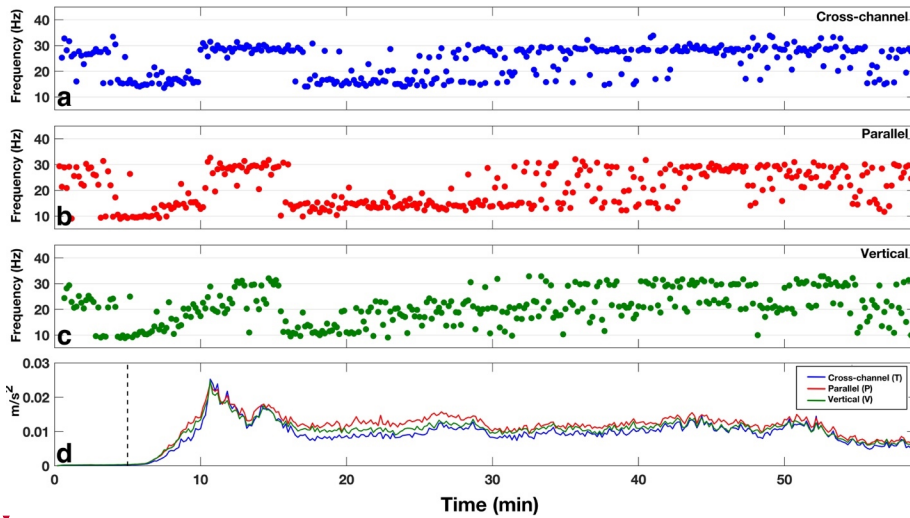
Formatted: Line spacing: Double

Deleted: , blue dots

Deleted: ,

Deleted: red dots

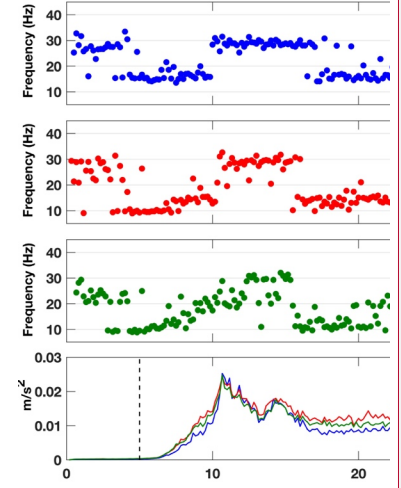
281



282

283 Figure 4 Peak spectral frequencies for TRAN (28 km from source) for **a)** cross-channel (blue), **b)** flow parallel (red),
 284 and **c)** vertical (green) directions. Bottom row **(d)** depicts the RMS amplitude of the lahar color coded to the same
 285 colors as the PSF. The dashed vertical line marks the timing of the lahar front passing the monitoring station. All
 286 PSFs and RMS amplitudes were calculated using 10 s time windows.

Deleted: In the vertical component (Figure 5, green dots), the PSF remains concentrated around ~28 Hz, only varying just prior to the arrival of the lahar and during the highest energy stage of the lahar (25-40 min).

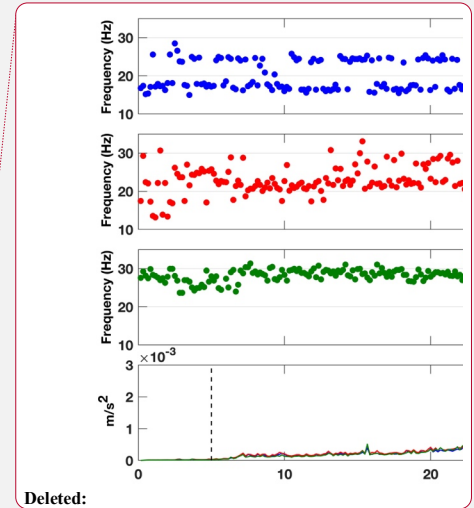
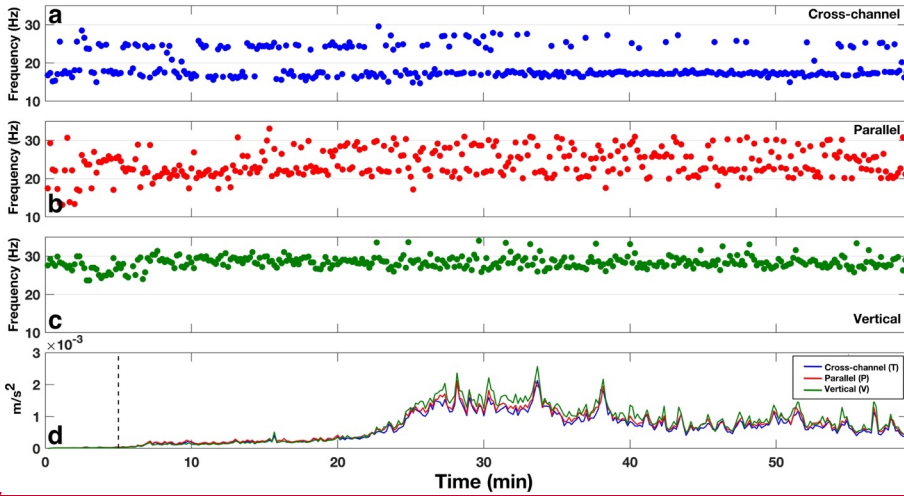


Deleted:

Deleted: dots

Deleted: dots

Deleted: dots



Deleted:

Deleted: dots

Deleted: dots

Deleted: dots

295

296 Figure 5 Peak spectral frequencies for COLL (83 km from source) for a) cross-channel (blue), b) flow parallel (red),
 297 and c) vertical (green) directions. Bottom row (d) depicts the RMS amplitude of the lahar color coded to the same
 298 colors as the PSF. The dashed vertical line marks the timing of the lahar front passing the monitoring station. All
 299 PSFs and RMS amplitudes were calculated using 10 s time windows.

300 3.2 Directionality

301 When recording mass flows with 3-component sensors, the directionality may be examined due
 302 to the sensor being able to record signals in the two horizontal directions. The directionality
 303 ratio allows for the determination of which horizontal component has stronger energy over the
 304 course of the recording window. This is possible because, in channel side deployments for mass
 305 flow monitoring systems, the sensor is either installed so that the North component is aligned
 306 to be parallel and the East component aligned as perpendicular to the flow, or the components
 307 are rotated during the data processing stage to align with the channel orientation.

Deleted: can be

308 Furthermore, with the channel side installations, attenuation factors can mostly be ignored
 309 due to the close proximity to the channel and energy output of the flow event. The

315 directionality ratio (DR) can be defined as the cross-channel amplitude divided by the flow
316 parallel amplitude. A DR > 1 indicates that the cross-channel amplitude is larger than that of the
317 flow parallel, and vice-versa for a DR < 1. Directionality ratios have been used in the past to
318 show rheology changes within flows, where the DR increases when streamflow transitions into
319 a lahar (Walsh et al., 2020), and have been hypothesized to be an indicator for flow properties
320 such as sediment concentration, wetted perimeter, and/or amount of particle collisions within
321 a lahar (Doyle et al., 2010).

322 The directionality ratios estimated from 10 s non-overlapping running time windows of the RMS
323 amplitudes at each seismic station for the 18 March 2007 lake-breakout lahar are shown in
324 Figure 6. The DR for RTMT (Figure 6a) displays a DR <= 1 (0.8-1.0) pre-lahar, then decreases
325 (0.7-0.8) as the lahar arrives at the recording station (Figure 6, dashed line), then as soon as the
326 lahar head arrives, the DR increases to above DR = 1 for ~2 min. After the peak lahar flood pulse
327 passes RTMT, the DR then proceeds to decrease below a DR = 1 for the rest of the recording
328 window. Similar to RTMT, the DR for TRAN starts out with a DR < 1 (0.7-0.8) and as the lahar
329 front passes, the DR similarly decreases to 0.6-0.7 before increasing to a DR > 1 for ~5 min
330 when the lahar is at peak energy output starting at about the 10 min mark (Figure 6d, red line).
331 After the passing of the peak energy, the DR for TRAN decreases below 1 again for the
332 remainder of the recording window. Further down the channel at COLL (Figure 6c), the DR
333 before the lahar arrives has a wide range of values between 0.8-1.2. When the front of the
334 lahar passes (Figure 6, dashed line), the DR stabilizes between 0.8-1, before increasing slightly
335 when the peak energy of the lahar passes the monitoring site at about the 25 min mark.

Deleted: for warning purposes

Deleted: for

Deleted: 10 s running time windows

Deleted:

Deleted: around 1

Deleted: right before

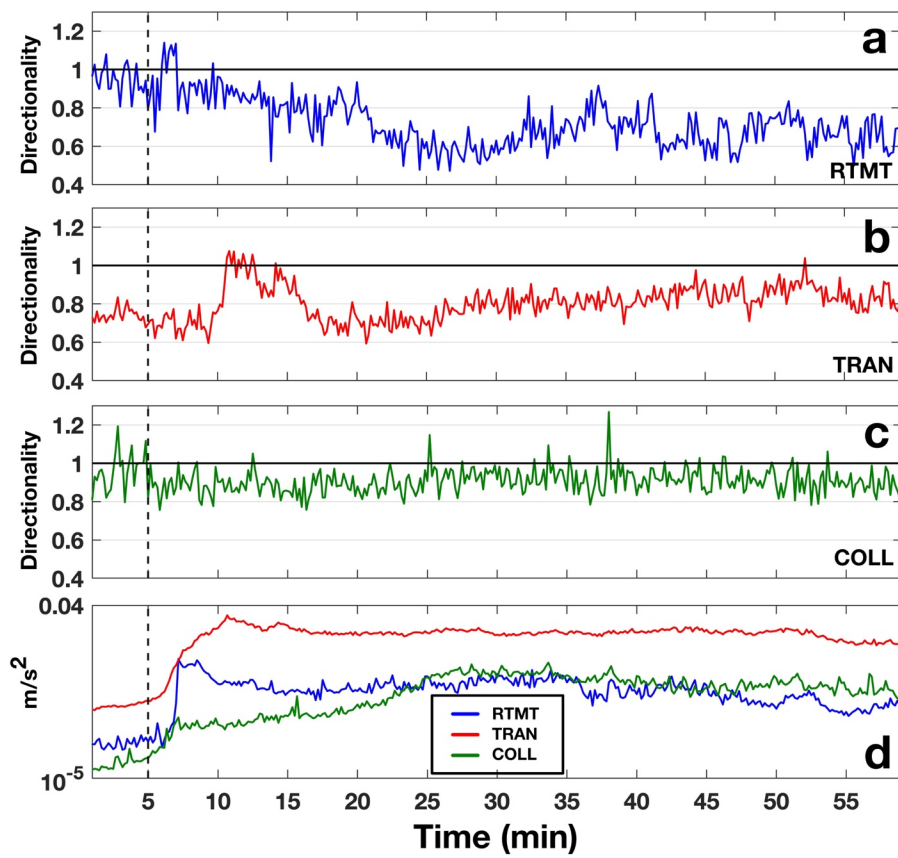
Deleted: passes

Deleted: initial

344

345

346



347

348 Figure 6 Directionality ratio plots over time for RTMT (a), TRAN (b), and COLL (c). Vertical RMS seismic signals for
349 the three stations are plotted in (d) where blue is RTMT, red is TRAN and green represents COLL. The dashed
350 vertical lines mark the timing of the lahar front passing the monitoring station. All DRs and RMS amplitudes were
351 calculated using 10 s time windows.

352 **4. Discussion**

353 **4.1 Frequency constraints**

354 In order to obtain an understanding if PSFs are able to properly describe the lahar dynamics (i.e.
355 the weight of the spectral amplitude at the PSF), frequency constraints must be analyzed. To
356 complete this, normalized spectrograms along with spectral centroidal frequency (SCF) and
357 spectral spreads are computed (e.g. Rubin et al., 2012; Saló et al., 2018). The normalized
358 spectrograms are estimated by normalizing (using the maximum) the spectral amplitude for
359 each 10 second time window of the lahar individually. By normalizing each time window, ranges
360 of dominant frequencies can be visualized. SCFs are used because they represent the weighted
361 average of the spectra, and yield the location (i.e. frequency) of the center of the spectral mass.
362 The SCF of each time window is estimated similar to that of Saló et al. (2018), in which:

363
$$SCF = \frac{\sum_{f_1}^{f_2} f * A(f)}{\sum_{f_1}^{f_2} A(f)} \quad (1)$$

364 where f is the frequency and $A(f)$ is the spectral amplitude associated with each frequency bin.

365 The spectral spread measures the width of the spectral energy around the SCF (i.e. standard
366 deviation), thus yielding information about the quality of the PSFs (e.g. Rubin et al., 2012;
367 Giannakopoulos and Pikrakis, 2014; Saló et al., 2018). Spectral spread can be estimated by:

368
$$SS = \sqrt{\frac{\sum_{f_1}^{f_2} (f - SCF)^2 * A(f)}{\sum_{f_1}^{f_2} A(f)}} \quad (2)$$

Deleted:

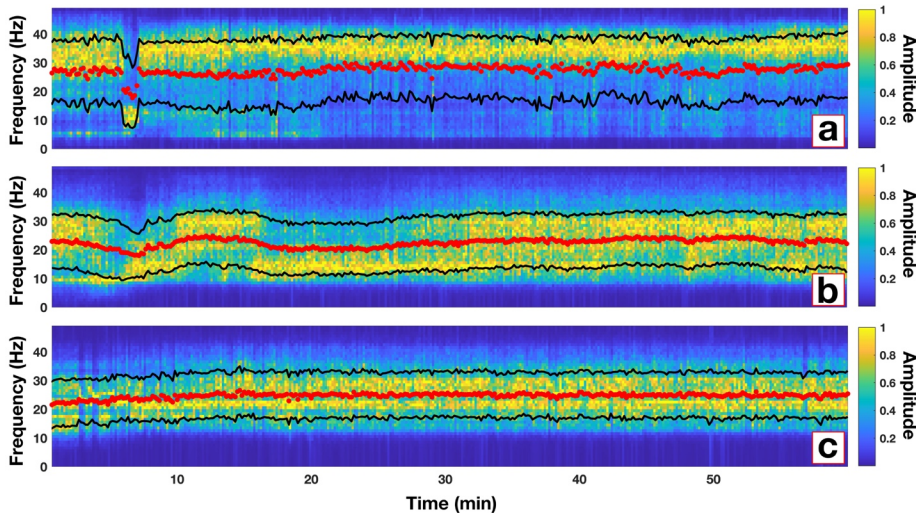
370 The computed normalized spectrograms along with SCFs and spectral spreads for each of the
371 three monitoring stations are shown in Figure 7. For simplicity and comparison, only the flow
372 parallel data are shown. The normalized spectrograms for every station and component can be
373 seen in Figures S1-S3, as well as the values in Table S1.

374 The normalized spectrogram for RTMT (Figure 7a) yields very similar results to that of the PSF
375 (Figure 3b), where most of the higher spectral amplitudes are at the same frequencies as those
376 of the PSF. Notably, the low ~10 Hz signal immediately before the arrival of the head of the
377 lahar is not only seen in the dominant normalized spectra, but also through the decrease in SCF.

Deleted: ate

378 Additionally, the PSFs at these time windows are contained within the spectral spread (Figure
379 7a, black lines). For TRAN, the normalized spectrogram (Figure 7b) is again, very similar to the
380 PSF in Figure 4b. The SCF mirrors the pattern of the PSF with higher frequencies for the
381 streamflow, a decrease for the front of the lahar, increase for the head of the lahar, decrease
382 after the passing of the head, and finally a slight increase later in the lahar body. The
383 normalized spectra yields this same pattern, with the late lahar body displaying the only
384 timeframe with increased spectral amplitude distributed throughout the spectral spread (Figure
385 7b, after 30 min). This most likely explains the bimodal distribution of PSFs for TRAN in Figure 4
386 after the ~30 min mark. Continuing, the normalized spectrogram for COLL (Figure 7c), also
387 shows similarities to that of the PSFs in Figure 5b. The PSFs for COLL range between ~20-30 Hz
388 with a slight bimodal pattern. This same pattern can be seen where the higher spectral
389 amplitudes are located (Figure 7c). Furthermore, the SCF for COLL splits the PSF range and stays
390 at ~25 Hz during the bimodal phase of the PSF. Overall, with the analysis of the normalized

392 spectrograms, SCFs and spectral spreads, we confirm that the use of PSFs to describe mass flow
393 dynamics is concise for the 18 March 2007 lake-breakout lahar.



394
395 *Figure 7 Normalized spectrograms for the flow parallel direction for each of the three monitoring sites along the*
396 *Whangaehu channel. Red dots represent the spectral centroidal frequency and black lines show the range of the*
397 *spectral spread. Note, normalized spectrograms for the other directions can be seen in Figures S1-S3.*

398 4.2 Evolution of lahar signals

399 4.2.1 Phase 1 evolution

400 A lahar propagating down channel can bulk up by collecting material from erosion or through
401 the coalescing of multiple pulses to shorten the total length of the lahar (Procter et al., 2010;
402 Doyle et al., 2011). Lahars can also debulk by depositional means or by the natural elongation
403 of the lahar as it progresses down channel (Doyle et al., 2011; Lube et al., 2012). Considering
404 the 18 March 2007 lake-breakout lahar was a large pulse of water that only mixed with the
405 existing streamflow and contained no juvenile material, examining the seismic signatures along

Formatted: Font: Not Bold, Italic

406 the flow path can be used to characterize the evolution and transformation of a lake-breakout
407 event from outburst flood to hyperconcentrated flow and beyond. At RTMT, the seismic
408 signature is dominated by the flow parallel direction (Figure 3d) with > 30 Hz PSF (Figure 3b).
409 The exception to this is the timeframe immediately before the head of the lahar passes, when
410 the PSF decreases to ~10 Hz. This low frequency signal can be seen also at TRAN (Figure 4a-c)
411 and in the flow parallel direction at COLL (Figure 5b). However, at COLL the PSF is ~20 Hz
412 instead of 10 Hz as recorded at RTMT and TRAN, most likely due to differing flow properties at
413 83 km from source. This low PSF before the head of the lahar arrives at each station probably
414 represents the supercharged stream flow pulse (bow wave, Figure 2c) that is pushed in front of
415 the head of the lahar (i.e. phase 1, see section 1.1) as described by Cronin et al. (1999) where
416 they noticed these same pulses in front of lahar heads for three lahars on Mt. Ruapehu in 1995.
417 Conversely, this frontal pulse could be from the uplift of streamflow from the faster moving
418 underflow of the lahar (Manville et al., 2000). Furthermore, the low frequency zone before the
419 head of the flow lengthens as the lahar progresses downstream, suggesting that lahar
420 elongation can also be seen in the seismic frequency domain (~1 min at RTMT, ~5 min at TRAN).
421 The ~10 Hz PSF may be explained by flow processes (e.g. frictional resistance of the flow by the
422 channel, waves at free surface) (Schmandt et al., 2013; Barriere et al., 2015; Bartholomaeus et
423 al., 2015) and could be due to the flow at this stage being more sensitive to discharge (e.g.
424 increase in shear velocity and/or flow depth) (Gimbert et al., 2014; Schmandt et al., 2017;
425 Anthony, et al., 2018) or in the case of the underflow hypothesis, frictional sliding on the
426 channel bed (Huang et al., 2004). The frontal surge or phase 1 of the lahar can be seen in the
427 DR (Figure 6) as well. For every station along the channel the DR has a slight drop when phase 1

Deleted: (Figure 3)

Deleted: component

Deleted: ,

Deleted: red dots

Deleted: as in

Deleted: the

Deleted: could

435 passes the recording station (Figure 6, dashed line). The elongation of phase 1 also ~~has a~~
436 ~~correlation with distance from source~~, where the dip in the DR ~~lasts for~~ only ~1 min ~~at~~ RTMT, ~5
437 min ~~at~~ TRAN, and approximately 20 min ~~at~~ COLL. The reason the DR decreases during phase 1
438 for the 2007 lahar could be due to the parallel component being more sensitive to flow
439 processes than bedload forces (Barriere et al., 2015; Roth et al., 2016). During phase 1
440 discharge increases, sediment concentration is low (Cronin et al., 1999), and streamflow
441 dominates resulting in a low DR (e.g. Doyle et al., 2010). The low DR can also be seen before the
442 arrival of phase 1, due to streamflow already occurring in the channel. The higher flow parallel
443 amplitude over cross-channel amplitude for streamflow has also been noted in the past for
444 lahars at Volcán de Colima, Mexico (Walsh et al., 2020).

445 4.2.2 Phase 2 evolution

446 Following the low PSF phase 1 (i.e. front of the lahar), the peak seismic amplitude occurs (~~flow~~
447 ~~head~~). The peak seismic amplitude for RTMT (~~Figure 3d~~) is accompanied by an increase to
448 higher PSFs > 30 Hz (Figure ~~3a-c~~, 7a). PSFs > 30 Hz have been shown in the past to be either
449 dominated by turbulence or bedload transport (e.g. Gimbert et al., 2014; Roth et al., 2016). The
450 2007 lake-breakout lahar has been described as a hyperconcentrated streamflow (e.g. Procter
451 et al., 2010b) with low sediment concentration, especially early on before the lake water
452 captured enough material to bulk up ~~and transform~~. At RTMT, which was only 7.4 km from
453 source, the lahar had not fully bulked up yet and was in a net depositional regime (Procter et
454 al., 2010a). Due to the conditions of the lahar at RTMT (~~e.g. Figure 2a~~), we surmise the higher
455 PSF content for the peak seismic amplitude is dominated by turbulent-flow-induced noise.

Deleted: can

Deleted: be seen

Deleted: is

Deleted: for

Deleted: for

Deleted: for

Formatted: Font: Italic

Deleted: into a full 4-phase lahar (see section 1.1)

463 Furthermore, the higher PSF content at RTMT (>30 Hz) compared to TRAN and COLL (~30 Hz)
464 could be due to the angle of the slope at the recording stations. Gimbert et al. (2014) noted
465 that turbulence noise will dominate over bedload-induced noise on steeper slopes due to an
466 increase in shear velocity. If we use the average flow velocities as a comparison, the lahar at
467 RTMT (9.3 m/s) flowed faster than at the other two stations (TRAN, 5.6 m/s; COLL, 4.8 m/s).
468 Further down the channel at TRAN, the PSF for the peak seismic amplitude is ~30 Hz for all
469 three components (Figure 4a-c, Table S1). Again, this high PSF may be attributed to turbulence,
470 as seen by the images taken at TRAN (Figure 2d). The difference at TRAN is the duration of the
471 higher PSF, where at RTMT the high PSF stays throughout the entirety of the recording window,
472 at TRAN the high PSF only last for ~5 min (Figure 4a-c, ~11-16 min). The difference at TRAN
473 could be from the evolution of the lahar. By time the lahar reached the monitoring station at
474 TRAN (28 km from source) the lahar was fully bulked up and had the properties of a traditional
475 four phase lahar as described by Scott (1988) or Cronin et al. (1999) (Figure 2c-e, see section
476 4.2.3). By time the lahar reached COLL 82 km from source (Figure 5), the peak seismic
477 amplitude is associated with PSFs between 15-30 Hz, with bimodal patterns in the horizontal
478 components and a tighter spread in the vertical component (~27-29 Hz). At COLL, the lahar had
479 converted into a plug-like flow with lower turbulence and hence the higher PSFs are most likely
480 associated with bedload transport (Figure 2f). Furthermore, Burtin et al. (2010) and Roth et al.
481 (2016) noted that when the vertical component has greater seismic amplitudes than the
482 horizontal components, bedload dominates. This same amplitude feature can be seen at COLL
483 (Figure 5d, past ~25 min) where the vertical energy is greater than each of the horizontal
484 components. The bimodal frequency pattern of the horizontal components (Figure 5a,b) is

Deleted: can

Deleted: length

Deleted: and seismic amplitude

Deleted: , bottom panel

Deleted:

490 likely to be the recording of both water-flow noise (lower PSF) and bedload transport (higher
491 PSF). This also explains why the vertical component does not show the same bimodal frequency
492 pattern. Barriere et al. (2015) described the parallel component as being more sensitive to flow
493 properties (e.g. discharge, depth, shear velocity), and Doyle et al. (2010) noted that the cross-
494 channel component is likely dominated by the amount of turbulence (water and particles acting
495 on the channel walls), thus the reasoning behind the differing PSF patterns between
496 components. This PSF feature is similar to the lahars recorded by Walsh et al. (2020), where the
497 cross-channel PSF is confined within a narrow band around 15-20 Hz and the flow parallel PSF is
498 more bimodal (10-40 Hz). At COLL, the cross-channel PSF (Figure 5a) is dominated by PSFs at
499 ~18 Hz (lower than vertical component at ~28 Hz, Figure 5c), with the flow parallel between 20-
500 30 Hz (Figure 5b).

Deleted: turbulence or flow properties

501 The DR at the peak seismic amplitude for all three recording stations increases (Figure 6). The
502 DR for both RTMT and TRAN increases to DR > 1. Doyle et al. (2010) noted that higher wetted
503 perimeters will increase the DR, which can be seen at TRAN for the 18 March 2007 lake-
504 breakout lahar (Figures 2d, 6, peak DR/RMS amplitude). Conversely, the DR decreases after the
505 peak seismic amplitude while the wetted perimeter is still high (Figure 2d,e). While the wetted
506 perimeter may be a factor in increasing cross-channel energy and thus the DR, the more likely
507 explanation for the 18 March 2007 lahar might be the higher level of particle collisions and
508 turbulence at the peak seismic amplitude. More turbulent particle collisions would increase the
509 DR (e.g. Doyle et al., 2010) due to more lateral excitation within the flow and against the
510 channel walls increasing the cross-channel signal. The increase in collisional energy also relates
511 well with the PSF, as higher PSF correlates to an increase in the amount of interflow collisions

Deleted: is true

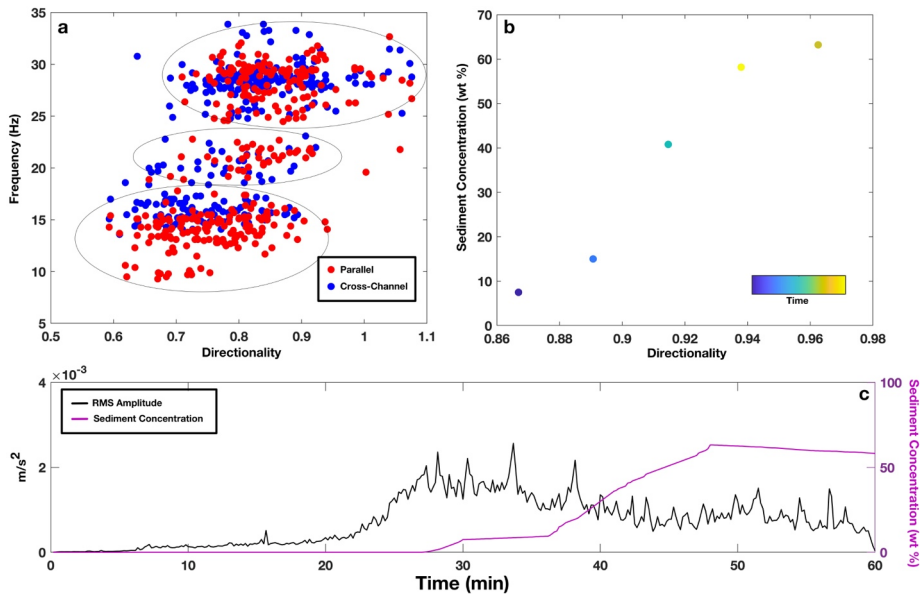
Deleted: Figure

Deleted: ,

Deleted: Also, at COLL the DR only increases slightly with the seismic amplitude.

518 as shown by Huang et al. (2004), and may also explain the slight increase in DR overall when the
519 PSF increases, (Figure 8a). The DR for COLL (Figure 6c) during this same timeframe probably is
520 not due to the amount of particle collisions due to the plug-like flow (Figure 2f), but rather the
521 increase in sediment concentration (Figure 8c). As the sediment concentration increases at
522 COLL the DR starts to increase as well (Figure 8b). Similar to Doyle et al. (2010), COLL yields a
523 correlation between DR and sediment concentration ($R^2=0.95$, Figure 8b), where higher DRs
524 indicate higher concentrations of sediment contained in the flow. Lastly, as noted above, DRs
525 may correlate with PSF or at least indicate differing processes taking place within the flow
526 (Figure 8a). Lower PSF would produce lower DRs because low PSF are more sensitive to water-
527 flow processes (hence higher parallel energy), whereas higher PSFs would produce higher DRs
528 due to higher PSF being dominated by sediment, particle collisions and turbulence (higher
529 cross-channel energy) (Figure 8a).

Deleted: why DRs correlate well with PSF



531

532 Figure 8 Plots of (a) comparing PSF and DR at TRAN, (b) sediment concentration and DR at COLL ($R^2=0.95$), and (c)
 533 seismic amplitude (black line) with sediment concentration (purple line) depicting the lag in sediment at COLL. Note
 534 on (a) parallel (red dots) and cross-channel (blue dots) PSF display three different zones (black circles). Also note
 535 that at COLL the first sediment concentration measurement did not occur until the 30 min mark.

Deleted: correlation between
 Formatted: Font color: Text 1

536 4.2.3 Development of flow phases at TRAN

Formatted: Font: Italic

537 While the lahar at RTMT was a large outburst flood/sediment-laden flow, and at COLL a plug-
 538 like flow, at TRAN the 18 March 2007 lahar was a dynamic bulked up jahar (see Figure 2b-e).

Deleted: "traditional"

539 The evidence for this is in the PSF content for TRAN (Figure 4a-c) compared to the other two
 540 monitoring sites (Table S1). At TRAN the PSF has a step-up step-down pattern for the first 30
 541 min of the lahar passing, and then transitions to a bimodal or wide PSF range for the rest of the
 542 recording window. As noted above, the low PSF preceding the lahar head arrival is thought to
 543 be due to a sensitivity to water transport properties (Figure 2c, phase 1). The increase to higher
 544 PSFs during the peak seismic amplitude may be from particle collisions and/or higher

547 turbulence (Figure 2d, transition from phase 1 to 2). After the maximum seismic amplitude at
548 TRAN (Figure 4, ~10-15 min), the PSF decreases to 10-20 Hz. This drop in PSF after the highest
549 stage and amplitude could be from a more water-flow dominate regime (seen in the increased
550 parallel amplitude, Figure 4d, and decrease in DR, Figure 6b), where turbulence decreases
551 (Figure 2e), discharge is still high, and the peak sediment concentration has not occurred yet
552 (e.g. Cronin et al., 1999). Likewise, the decrease may also be from greater frictional sliding on
553 the channel bed (Huang et al., 2004). After the decrease to 10-20 Hz PSFs, the PSF displays a
554 bimodal or wide frequency range at ~28 min (Figure 4a-c, 7b). As aforementioned for COLL, this
555 PSF pattern could be from both bedload- and water-flow-induced noise. This timeframe (phase
556 3) is also where the peak sediment concentration would be (not recorded at TRAN), as noted by
557 Cronin et al. (1999), and thus the PSF would show more bedload high PSF. This hypothesis also
558 compares well with the DR (Figure 6b), where the cross-channel energy increases starting at
559 ~25 min indicating that the sediment concentration may be increasing (Doyle et al., 2010).
560 Finally, the wide PSF range later in the recording window (Figure 4) could also result from the
561 lahar having two distinct layers as described by Cronin et al. (2000), where there is a wide more
562 dilute finer grain top layer and a channelized sediment-rich layer on the bottom. The two layer
563 model can apply to TRAN because the lahar at this monitoring station overtook the channel
564 (Figure 2d,e) and proceeded to flow horizontally outward forming the surface layer described
565 by Cronin et al. (2000).

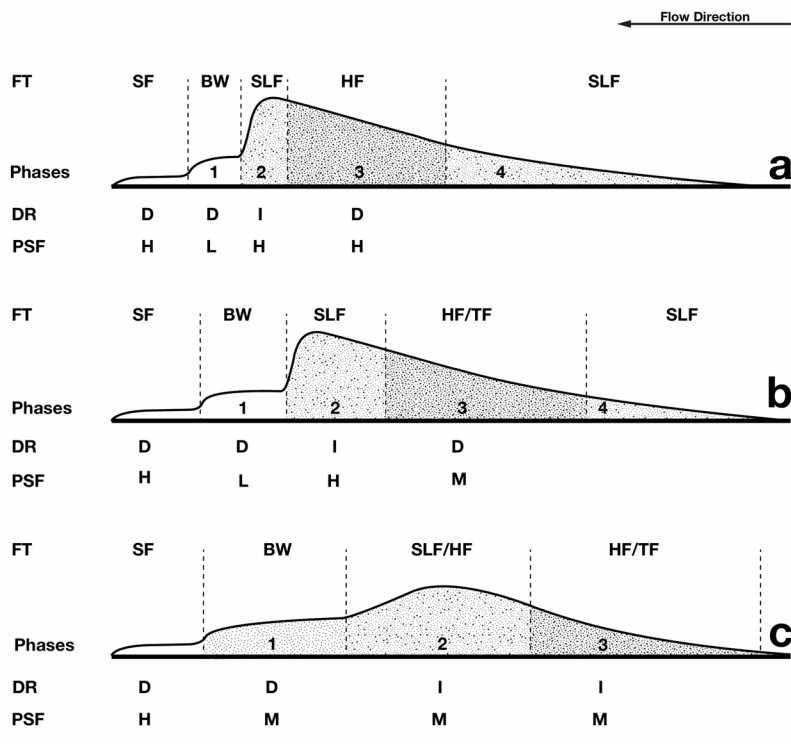
566 4.3 Implications for monitoring

- Deleted: transport
- Deleted: ed
- Deleted: ,
- Deleted: which can be
- Deleted: (
- Deleted: 8a
- Deleted: .
- Deleted: T
- Deleted: Furthermore, this PSF range could simply indicate a decrease in turbulence (Figure 2e).
- Deleted: transport

578 The main goal of this research is to contribute in defining better monitoring criteria for
579 dangerous mass flow events. The data described above is part of a larger collection of
580 monitoring data collected over the entire length of the Whangaehu channel consisting of 21
581 monitoring sites and years of preparation (e.g. Manville and Cronin, 2007; Keys and Green,
582 2008). Due to this, the ability to accurately estimate the properties of the lahar at various
583 stages along its path is possible. When it comes to flow events of any size, the ability to
584 understand how the dynamics change with distance along the channel is important for warning
585 and future hazard mitigation. We show here that a lake-breakout event can start out as an
586 outburst flood, bulk up into a hyperconcentrated flow, then eventually elongate and entrap
587 enough sediment to transform into a plug-like slurry flow. Each of these flow types yields
588 differing PSF ranges and patterns due to the relationship between the channel geometry,
589 sediment concentration, turbulence, and bedload transport. While the lahar at different
590 stations along the channel may have differing PSF content, we also show that the lahar
591 elongates and a predictable model (e.g. Cronin et al., 1999) can be used with and shown in the
592 seismic data. Being able to apply such a model may yield some relevance of universality in
593 terms of warning systems at different distances away from the mass flow source. Whereas,
594 shown above, the flow phases at each monitoring station can be seen, but at differing lengths
595 and times in the seismic signal (e.g. Figure 6). To better visualize this concept, conceptual
596 models based off of the Cronin et al. (1999) models are created for each of the three seismic
597 stations for the 18 March 2007 lahar (Figure 9). In the conceptual models for the 2007 lahar,
598 the aforementioned elongation of the frontal pulse or bow wave (phase 1) and head of the

Deleted: ,

600 lahar (phase 2) is shown, along with the differences and similarities between the properties of
 601 the lahar at the three seismic monitoring sites.



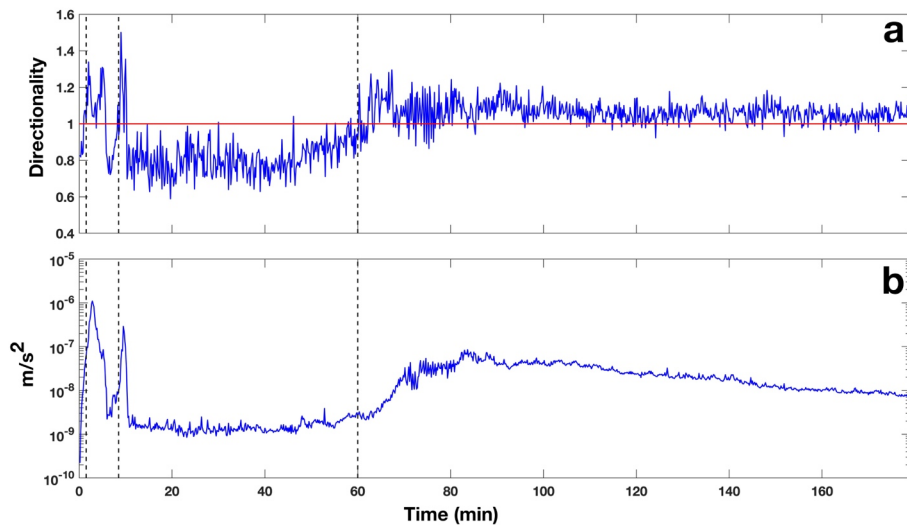
602
 603 *Figure 9 Conceptual models for the 18 March 2007 lahar at each of the three monitoring stations along the*
 604 *Whangaehu channel depicting flow type and the estimated seismic properties at each flow phase. a) RTMT 7.4 km*
 605 *from source, b) TRAN 28 km from source, and c) COLL 83 km from source. Flow types (FT) are as followed;*
 606 *streamflow (SF), bow wave streamflow (BW), hyperconcentrated flow (HF), Transitional flow (TF), and sediment-*
 607 *laden streamflow (SLF). Note, decreased (D), increased (I), high (H), low (L), and mixed (M) are notations for*
 608 *directionality ratios and peak spectral frequency estimates. See Table S1 for value ranges for each property.*

609 Another implication for future warning is the implementation of 3-component sensors and the
 610 use of DRs for channels that have streamflow. Walsh et al. (2020) showed for lahars flowing in

611 La Lumbre channel at Volcán de Colima that the DR for streamflow is <1 and then increases
612 when the [head of the](#) lahar arrives. This same feature can be seen at each of the three
613 monitoring sites for the 18 March 2007 event (Figure 6) indicating differing flow types will still
614 show this DR pattern within the same flow and at other channels. To further show this, there
615 were three natural non-lake-breakout eruption-based lahars that occurred in the Whangaehu
616 channel in September 2007 (for more details on the lahars see Cole et al., 2009; Kilgour et al.,
617 2010) and recorded on the seismometer at RTMT. The DR for the September events starts with
618 streamflow with a $DR < 1$ and when the first lahar arrives the DR increases to >1 and as the
619 lahar fully passes, the DR decreases to <1 again (Figure 10a). As the second lahar arrives at
620 RTMT (Figure 10, second dashed line), the DR increases to >1 again. After the second lahar
621 passes the DR decreases once again back below $DR < 1$. Finally, as the third lahar arrives (Figure
622 10, third dashed line) the DR yet again increases above 1 for the entirety of the event.

623 For many mass flows and especially those that flow into channels with preexisting streamflow,
624 the peak seismic amplitude does not always coincide with the arrival of the mass flow, and thus
625 may not be the most reliable for event detection or warning ([e.g. Arratano and Moia, 1999;](#)
626 [Cole et al., 2009](#)). These observations may be due to a frontal surge, the lag in sediment
627 concentration or differences in peak amplitude with peak discharge. Phase 1 (frontal
628 streamflow surge) of the model proposed by Cronin et al. (1999) was based on a
629 hyperconcentrated flow interacting with streamflow, but has also been shown for debris flows
630 as well (e.g. Arratano and Moia, 1999). Arratano and Moia (1999) showed at Moscardo Torrent,
631 Italy, through a hydrograph that there was a precursory surge ahead of the debris flow that was
632 not seen in the seismic record. Similarly, at Ruapehu, for the 18 March 2007 lahar, at each of

633 the three stations there is little evidence or rise in the seismic amplitude that would indicate
634 that there was a precursory surge or phase 1 (Figures 3-5, bottom panel), which could be
635 problematic for detection methods that use amplitude thresholds or short-time-average vs
636 long-time-average (STA/LTA) algorithms. Conversely, the surge ahead of the lahar can be seen
637 in both the PSF analysis (drop to low frequencies) and in the DR (decrease in DR) right before
638 the peak seismic amplitude arrives. This shows that when monitoring for future events that not
639 only the amplitude should be used, but other analysis (e.g. PSF, DR) as well, otherwise there
640 could be a delay in the detection of an event.



641
642 *Figure 10 (a) Directionality ratio for the time sequence of the three lahars that occurred on 25 September 2007. (b)*
643 *RMS amplitude of the seismic record at RTMT during the timing of the three September lahars. Note that the black*
644 *dashed lines represent the timing of each lahar arriving at the monitoring site.*

645 Using all three components of the seismometer can be very beneficial in lahar monitoring. The
646 above-mentioned DR analysis can only be completed with horizontal recording, and analyzing

647 PSF in each component can yield critical information about the flow properties and dynamics.
648 Examining the seismic amplitude differences can generate significant discoveries, for example,
649 when the vertical component is stronger than the horizontal components, bedload may
650 dominate over turbulence noise (Burtin et al., 2010). Greater flow parallel signals may indicate
651 higher water transport noises (Barrier et al., 2015), while higher cross-channel signals could be
652 caused by increased interflow particle collisions and flow-channel wall interactions (Doyle et al.,
653 2010). While using the differences in each component can be useful, there are also some
654 concerns. Channel geometry and bed conditions can alter the seismic signal (e.g. Coviello et al.,
655 2019; Marchetti et al., 2019). Additionally, the flow parallel direction can be influenced by the
656 lahar that has already passed, the lahar at the station and the lahar arriving. Furthermore, the
657 tilt of the seismometer may play a large role in determining which component is stronger (e.g.
658 Anthony et al., 2018). In the case of the 18 March 2007 lahar a large pulse of water passed the
659 monitoring stations which may explain why the parallel component is stronger than the other
660 two components at RTMT (Figure 3d) and TRAN (Figure 4d). At COLL, the lahar had elongated,
661 lost energy, and thus shows more decreased flow parallel energy compared to the previous two
662 stations (Figure 5d). In the cross-channel direction, if a flow overtops the channel, the
663 amplitude would presumably be dampened. This may be the case at TRAN where both the flow
664 parallel and vertical directions are more energetic than the cross-channel amplitude after the
665 passing of the head and breaking out of the channel occurred (Figures 2d, 4d). Another concern
666 when using the horizontal components of a seismometer are the effects shallow layers may
667 have on the site response of the sensor. This is especially true when a sensor is installed on soft
668 or loose sediment (e.g. soil, fluvial/alluvial deposits). To test for potential effects by shallow layer

Deleted: s

Deleted: and

Deleted:

Deleted: larger

Deleted:

Deleted: bottom row

675 fundamental frequencies, H/V analysis of ambient noise (streamflow dominant) was conducted
676 (see Supplementary material). For RTMT, the H/V results depict a broad frequency peak
677 between 5-15 Hz with a local maximum at ~8 Hz (Figure S4a). Comparing the H/V frequency
678 with the PSF of RTMT (Figure 3), the only overlap is when the front of the lahar passes the
679 station where the PSF decreases for ~1 minute before the head of the lahar arrives. The H/V
680 analysis for TRAN has a multi-broad-peak shape, with frequency peaks at ~14 and ~28-35 Hz
681 (Figure S4b). While these frequencies are similar to PSF values for TRAN (Figure 4), the H/V
682 analysis has no distinguishable fundamental frequency, contains large error, and no frequency
683 peak has a H/V amplification > 2. In order for a H/V frequency peak to be considered ideal,
684 generally the amplification must be greater than 2 and the standard deviation lower than a
685 factor of 2 (SESAME, 2004). The H/V amplification for COLL displays a broad frequency peak
686 between 13-18 Hz, with a local maximum at ~18 Hz (Figure S4c). Comparing the PSFs at COLL
687 (Figure 5), only the cross-channel direction has significant PSF values in the same frequency
688 range (~18 Hz band). With all three stations not yielding distinct H/V fundamental frequencies,
689 we surmise that the PSF content for the 18 March 2007 lake-breakout lahar is most likely
690 dominated by the large flow passing by the seismic sensor rather than large site amplification
691 effects from a shallow layer. While this may be the case, there is still the possibility that some
692 of the PSF values could be due to local effects and should not be considered in the lahar
693 analysis, e.g., the low PSFs at RTMT between 15-20 min (Figure 3a,b), at TRAN contributing to
694 some of the “jumping” in PSF content (Figure 4a-c), or in the mostly dominant 15-20 Hz PSF in
695 the cross-channel direction at COLL (Figure 5a). Conversely, SCF values at each station do not
696 reside in the broad H/V frequency range at any station (Figure 7), which may further support

Deleted: immediately before

Deleted:

Deleted: to

Deleted: frequency peaks

701 the hypothesis that almost all of the recorded frequencies are indeed produced by the lahar.
702 With the use of horizontal components becoming common in mass flow monitoring, future 3-
703 component analyses of mass flows should consider estimating H/V ratios or use other site
704 response methods (e.g. spectral ratio analysis) in order to identify whether near-surface
705 structures may affect the recorded flow data. Overall, all these concerns can and should be
706 tested to estimate potential error in 3-component methods. Nevertheless, using all three
707 components of the seismometer can enhance the productivity of warning systems, and if
708 possible, should be used instead of single component sensors.

709 Finally, implementation of these new results into new or existing mass flow warning systems
710 must be discussed. In an ideal setup, to remove any doubt about the recorded signal, machine
711 learning techniques should be used to separate the mass flow noise from other non-flow noises
712 (e.g. environmental, human induced, earthquakes). For instance, recently Wenner et al. (2021)
713 used a supervised random forest algorithm to classify differing sources in a debris flow setting.
714 Once the mass flow source has been classified, integrating automated DR and PSF analysis
715 would be quick and straightforward. Implementation of these techniques would be similar to
716 other seismic analysis or detection methods, such as a STA/LTA (e.g. Coviello et al., 2019) or a
717 number of frequency detection algorithms (e.g. Rubin et al., 2012) where real-time analysis of
718 set time windows are used to determine if there has been a change in the seismicity along the
719 channel. The system could be programed to identify changing features in the flow automatically
720 by analyzing the content of each window, as well as comparing previous time windows. The
721 analysis of continual data could then be feed into machine learning algorithms (e.g. Rubin et al.,
722 2012; Wenner et al., 2021) to increase the confidence of not only detection, but the

723 characterization of flow behavior. One of the main discoveries of this research was the
724 evolution of seismic signals produced by the lahar as the flow moved further from its source.
725 The changes in the seismic signal along with the flow characteristics may be able to help hazard
726 and forecast modeling through the use of numerical models (e.g. Mead et al., 2021). Modern
727 flow hazard assessment is based on numerical models that use potential energy equations of a
728 large non-changing mass sliding down slope with limited inputs for how the flow may evolve
729 over time as starting inputs. This can lead to errors in risk mitigation and hazard assessments.
730 The findings shown above on how the 18 March 2007 lahar evolved over 83 km at Mt. Ruapehu
731 will help to improve mass flow modeling in the future by enabling modelers to add constrains
732 or more inputs on how a mass flow might evolve, leading to improved forecasts and hazard
733 assessment.

734 **5. Conclusions**

735 At 23:18 UTC on 18 March 2007, Mt. Ruapehu produced the biggest lahar in New Zealand in
736 over 100 years causing 1.3×10^6 m³ of water to flow out of the Crater Lake and rush down the
737 Whangaehu channel flowing for over 200 km to the Tasman sea. Seismic analysis at three
738 monitoring locations along the channel (7.4, 28, and 83 km) yielded an understanding of how
739 flow type and processes of the lahar evolve with distance. The proximal lahar was a highly
740 turbulent outburst flood, which generated high PSF content in all three components. Further
741 along the channel after the lahar had bulked up and transformed into a multi-phase
742 hyperconcentrated flow, the PSF content was variable and showed changes in the flow
743 regime/phase. Finally, at the most distal monitoring station, the lahar had lost energy and

744 transformed into a slurry-type flow where the PSF content became more bedload-dominant.
745 Additionally, directionality ratios from all three sites along with data from additional lahars
746 yielded strong evidence that DRs can be used for warning systems when there is streamflow
747 present in the channel. Furthermore, PSF and DRs show evidence of a pre-lahar water pulse
748 that may be concealed in the raw seismic data, but has been observed visually. Ultimately, the
749 use of 3-component broadband seismic analysis for the 18 March 2007 lahar at Mt. Ruapehu
750 may lead to more accurate and advanced real-time warning systems for mass flows through the
751 use of frequency and directionality around the world.

Deleted: is

752 *Author Contribution*

753 BW performed seismic analysis and drafted the manuscript, CL organized and prepared data,
754 and JP created the visual location representation of the event. All participating authors
755 contributed to the discussions and editing of the draft of the manuscript, as well as approving
756 the final edition.

757 *Competing Interests*

758 The authors declare that they have no conflict of interest

759 *Data Availability*

760 The data used in this publication can be found at: Braden Walsh; Charline Lormand; Jon Procter;
761 Glyn Williams-Jones (2022), "18 March 2007 Mt. Ruapehu lahar seismic data,"
762 <https://thehub.org/resources/4890>.

763 *Acknowledgements*

765 This work was supported by the Resilience to Natures Challenges – New Zealand National
766 Science, volcano program of research. We would also like to thank all the people from Massey
767 University, Horizons Regional Council, NIWA, and the Department of Conservation that
768 collected data and set up monitoring locations all along the channel in preparation for and
769 during the lahar. A final special thanks to Kate Arentsen for editorial support.

770 **References**

771 Anthony, R., Aster, R., Ryan, S., Rathburn, S., Baker, M.: Measuring mountain river discharge
772 using seismographs emplaced within the hyporheic zone, *Journal of Geophysical Research:*
773 *Earth Surface*, 123, 210-228, 2018.

774 Arattano, M., Marchi, L.: Measurements of debris flow velocity trough cross-correlation of
775 instrumentation data, *Natural Hazards and Earth System Sciences*, 5, 137-142, 2005.

776 Arattano, M., Marchi, L., Genevios, R., Berti, M., Simoni, A., Tecca, P., Bonte, M.: Field
777 monitoring and real time management of debris flows, *European Project "Debris Flow Risk"*
778 *(N.ENV4960253), Final Report, 30, 1999.*

779 Arattano, M., Moia, F.: Monitoring the propagation of debris flow along a torrent, *Hydrological*
780 *Sciences- Journal des Sciences Hydrologiques*, 44(5), 811-823, 1999.

781 Barriere, J., Oth, A., Hostache, R., Krein, A.: Bed load transport monitoring using seismic
782 observations in a low-gradient rural gravel bed stream, *Geophys. Res. Lett.*, 42, 2294-2301,
783 2015.

Deleted: ¶

Formatted: Font: Italic

785 Bartholomaeus, T., Amundson, J., Walter, J., O'Neel, S., West, M., Larsen, C.: Subglacial discharge
786 at tidewater glaciers revealed by seismic tremor, *Geophys. Res. Lett.*, *42*, 6391-6398, 2015.

787 Burtin, A., Vergne, J., Rivera, L., Dubernet, P.: Location of river-induced seismic signal from
788 noise correlation functions, *Geophys. J. Int.*, *182*, 1161-1173, 2010.

789 Capra, L., Borselli, L., Barley, N., Ruiz, J., Norini, G., Sarocchi, D., Caballero, L., Cortes, A.:
790 Rainfall-triggered lahars at Volcan de Colima, Mexico: Surface hydro-repellency as initiation
791 process, *Journal of Volcanology and Geothermal Research*, *198*, 105-117, 2010.

792 Capra, L., Coviello, V., Borselli, L., Marquez-Ramirez, V., Arambula-Mendoza, R.: Hydrological
793 control of large hurricane-induced lahars: evidence from rainfall-runoff modeling, seismic and
794 video monitoring, *Nat. Hazards Earth Syst. Sci.*, *18*, 781-794, 2018.

795 Carrivick, J., Manville, V.: A fluid dynamics approach to modelling the 18th March 2007 lahar at
796 Mt. Ruapehu, New Zealand, *Bull. Volcanol.*, *71*, 153-169, 2009.

797 Cole, S., Cronin, S., Sherburn, S., Manville, V.: Seismic signals of snow-slurry lahars in motion: 25
798 September 2007, Mt Ruapehu, New Zealand, *Geophys. Res. Lett.*, *36*, L09405, 2009.

799 Coviello, V., Arattano, M., Comiti, F., Macconi, P., Marchi, L.: Seismic characterization of debris
800 flows: Insights into energy radiation and implications for warning, *Journal of Geophysical*
801 *Research: Earth Surface*, *124*, 2019.

802 Coviello, V., Capra, L., Vazquez, R., Marquez-Ramirez, V.: Seismic characterization of
803 hyperconcentrated flows in a volcanic environment, *Earth Surf. Process. Landforms.*, *43*, 2219-
804 2231, 2018.

805 Cronin, S., Neall, V., Jerome, L., Palmer, A.: Unusual "snow slurry" lahars from Ruapehu volcano,
806 New Zealand, September 1995, *Geology*, 24, 1107-1110, 1996.

807 Cronin, S., Neall, V., Jerome, L., Palmer, A.: Dynamic interactions between lahars and stream
808 flow: A case study from Ruapehu volcano, New Zealand, *GSA Bulletin*, 111(1), 28-38, 1999.

809 Cronin, S., Neall, V., Jerome, L., Palmer, A.: Transformation, internal stratification, and
810 depositional processes within a channelized, multi-peaked lahar flow, *New Zealand Journal of*
811 *Geology and Geophysics*, 43, 117-128, 2000.

812 Doyle, E., Cronin, S., Cole, S., Thouret, J.: The coalescence and organization of lahars at Semeru
813 volcano, Indonesia, *Bull. Volcanol.*, 72, 961-970, 2010.

814 Doyle, E., Cronin, S., Cole, S., Thouret, J.: Defining conditions for bulking and debulking in
815 lahars, *GSA Bulletin*, 123, 1234-1246, 2011.

816 Huang, C., Shieh, C., Yin, H.: Laboratory study of the underground sound generated by debris
817 flows, *Journal of Geophysical Research*, 109, F01008, 2004.

818 Iguchi, M.: Proposal of estimation method for debris flow potential considering eruptive
819 activity, *Journal of Disaster Research*, 14(1), 126-134, 2019.

820 [Giannakopoulos, T., Pikrakis, A.: Introduction to Audio Analysis, Chapter 4- Audio Features,](#)
821 [Academic Press, 59-103, 2014, <https://doi.org/10.1016/B978-0-08-099388-1.00004-2>.](#)

822 Gimbert, F., Tsai, V., Lamb, M.: A physical model for seismic noise generation by turbulent flow
823 in rivers, *Journal of Geophysical Research: Earth Surface*, 119, 2209-2238, 2014.

Formatted: Font: Italic

824 Keys, H., Green, P.: Ruapehu lahar New Zealand 18 March 2007: Lessons for hazard assessment
825 and risk mitigation 1995-2007, *Journal of Disaster Research*, 3(4), 284-296, 2008.

826 Kilgour, G., Manville, V., Della Pasqua, F., Graettinger, A., Hodgson, K., Joly, G.: The 25
827 September 2007 eruption of Mount Ruapehu, New Zealand: Directed ballistics, surtseyan jets,
828 and ice-slurry lahars, *Journal of Volcanology and Geothermal Research*, 191, 1-14, 2010.

829 Kogelnig, A., Surinach, E., Vilajosana, I., Hubl, J., Sovilla, B., Hiller, M., Dufour, F.: On the
830 complementariness of infrasound and seismic sensors for monitoring snow avalanches, *Nat.*
831 *Hazards Earth Syst. Sci.*, 11, 2355-2370, 2011.

832 Kuehnert, J., Mangeney, A., Capdeville, Y., Vilotte, J., Stutzmann, E., Chaljub, E., et al.: Locating
833 rockfalls using inter-station ratios of seismic energy at Dolomieu crater, Piton de la Fournaise
834 volcano, *Journal of Geophysical Research: Earth Surface*, 126, e2020JF005715, 2021.

835 Lube, G., Cronin, S., Manville, V., Procter, J., Cole, S., Freundt, A.: *Geology*, 40, 475-478, 2012.

836 Manville, V., Cronin, S.: Breakout lahar from New Zealand's crater lake, *EOS Transactions*,
837 88(43), 441-456, 2007.

838 Manville, V., White, J., Hodgson, K.: Dynamic interactions between lahars and stream flow: A
839 case study from Ruapehu volcano, New Zealand: Discussion and reply discussion, *GSA Bulletin*,
840 112(7), 1149-1152, 2000.

841 Marchetti, E., Walter, F., Barfucci, G., Genco, R., Wenner, M., Ripepe, M., McArdell, B., Price, C.:
842 Infrasound array analysis of debris flow activity and implications for early warning, *Journal of*
843 *Geophysical Research: Earth Surface*, 124, 567-587, 2019.

844 Massey, C., Manville, V., Hancox, G., Keys, H., Lawrence, C., McSaveney, M.: Out-burst flood
845 (lahar) triggered by retrogressive landsliding, 18 March 2007 at Mt Ruapehu, New Zealand – a
846 successful early warning, *Landslides*, 7, 303-315, 2010.

847 Mead, S., Procter, J., Kerezturi, G.: Quantifying location error to define uncertainty in volcanic
848 mass flow hazard simulations, *Nat. Hazards Earth Syst. Sci.*, 21, 2447-2460, 2021.

Formatted: Font: Italic

849 O'Connor, J., Clague, J., Walder, J., Manville, V., Beebee, R.: Outburst Floods, *Reference Module*
850 *in Earth Systems and Environmental Sciences*, Elsevier, 2020.

851 O'Shea, B.: Ruapehu and the Tangiwai disaster, *NZJ. Sci. Tech.* 36B, 174-189, 1954.

852 Pardo, N., Cronin, S., Palmer, A., Nemeth, K.: Reconstructing the largest explosive eruptions of
853 Mt. Ruapehu, New Zealand: Lithostratigraphic tools to understand subplinian-plinian eruptions
854 at andesitic volcanoes, *Bull. Volcanol.*, 74, 617-640, 2012.

855 Pierson, T., Janda, R., Thouret, J., Borrero, C.: Perturbation and melting of snow and ice by the
856 13 November 1985 eruption of Nevado del Ruiz, Colombia, and consequent mobilization, flow
857 and deposition of lahars, *J. Volcanol. Geotherm. Res.*, 41(1), 17-66, 1990.

858 Pierson, T., Scott, K.: Downstream dilution of a lahar: Transition from debris flow to
859 hyperconcentrated streamflow, *Water Resources Research*, 21(10), 1511-1524, 1985.

860 Procter, J., Cronin, S., Fuller, I., Lube, G., Manville, V.: Quantifying the geomorphic impacts of a
861 lake-breakout lahar, Mount Ruapehu, New Zealand, *Geology*, 38, 67-70, 2010.

862 Procter, J., Cronin, S., Sheridan, M.: Evaluation of Titan2D modelling forecasts for the 2007
863 Crater Lake break-out lahar, Mt. Ruapehu, New Zealand, *Geomorphology*, 136, 95-105, 2012.

864 Procter, J., Cronin, S., Fuller, I., Sheridan, M., Neall, V., Keys, H.: Lahar hazard assessment using
865 Titan2D for an alluvial fan with rapidly changing geomorphology: Whangaehu River, Mt.
866 Ruapehu, *Geomorphology*, 116, 162-174, 2010.

867 Procter, J. N., Cronin, S. J., Zernack, A. V., Lube, G., Stewart, R. B., Nemeth, K., & Keys, H.: Debris
868 flow evolution and the activation of an explosive hydrothermal system; Te Maari, Tongariro,
869 New Zealand. *Journal of Volcanology and Geothermal Research*, 286, 303-316, 2014.

870 Procter, J., Zernack, A., Mead, S., Morgan, M., & Cronin, S.: A review of lahars; past deposits,
871 historic events and present-day simulations from Mt. Ruapehu and Mt. Taranaki, New
872 Zealand. *New Zealand Journal of Geology and Geophysics*, 64(2-3), 479-503, 2021.

873 Roth, D., Brodsky, E., Finnegan, N., Rickenmann, D., Turowski, J., Badoux, A.: Bed load sediment
874 transport inferred from seismic signals near a river, *J. Geophys. Res. Earth Surf.*, 121, 725-747,
875 2016.

876 Rubin, M., Camp, T., Van Herwijen, A., Schweizer, J.: Automatically detecting avalanche events
877 in passive seismic data, 11th International Conference on Machine Learning and Applications, ,
878 IEEE, 1, 13-20, 2012.

879 Schimmel, A., Coviello, V., Comiti, F.: Debris-flow velocity and volume estimations based on
880 seismic data, *Natural Hazards and Earth System Sciences*, 2021.

Formatted: Font: Italic
Formatted: Font: Italic, Superscript
Formatted: Font: Italic

881 Schmandt, B., Aster, R., Scherler, D., Tsai, V., Karlstrom, K.: Multiple fluvial processes detected
882 by river side seismic and infrasound monitoring of a controlled floor in the Grand Canyon,
883 *Geophys. Res. Lett.*, 40(18), 4858-4863, 2013.

884 Schmandt, B., Gaeuman, D., Stewart, R., Hansen, S., Tsai, V., Smith, J.: Seismic array constraints
885 on reach-scale bedload transport, *Geology*, 45, 299-302, 2017.

886 Saló, L., Corminas, J., Lantada, N., Mata, G., Prades, A., Ruiz-Carulla, R.: Seismic energy analysis
887 as generated by impact and fragmentation of single-block experimental rockfalls, *Journal of*
888 *Geophysical Research: Earth Surface*, 123, 1450-1478, 2018.

889 Scott, K.: Origins, behavior, and sedimentology of lahars and lahar runout flows in the Toutle-
890 Cowlitz river system, *USGS Professional Paper*, 1988.

891 Surinach, E., Vilajosana, I., Khazaradze, G., Biescas, B., Furdada, G., Vilaplana, J.: Seismic
892 detection and characterization of landslides and other mass movements, *Natural Hazards and*
893 *Earth System Sciences*, 5, 791-798, 2005.

894 Walsh, B., Coviello, V., Capra, L., Procter, J., Marquez-Ramirez, V.: Insights into the internal
895 dynamics of natural lahars from analysis of 3-component broadband seismic signals at Volcán
896 de Colima, Mexico, *Front. Earth Sci.* 8, 542116, 2020.

897 Walsh, B., Jolly, A., Procter, J.: Seismic analysis of the 13 October 2012 Te Maari, New Zealand,
898 lake breakout lahar: Insights into flow dynamics and the implications on mass flow monitoring,
899 *J. Volcanol. Geotherm. Res.*, 324,144-155, 2016.

900 Wenner, M., Hibert, C., Van Herwijnen, A., Meier, L., Walter, F.: Near-real-time automated
901 classification of seismic signals of slope failures with continuous random forests, *Nat. Hazards*
902 *and Earth Syst. Sci.*, 21(1), 339-361, 2021.

Formatted: Font: Italic